Acta Materialia 207 (2021) 116668

Contents lists available at ScienceDirect

Acta Materialia

journal homepage: www.elsevier.com/locate/actamat

Density-based grain boundary phase diagrams: Application to Fe-Mn-Cr, Fe-Mn-Ni, Fe-Mn-Co, Fe-Cr-Ni and Fe-Cr-Co alloy systems

Lei Wang, Reza Darvishi Kamachali*

Federal Institute for Materials Research and Testing (BAM), Unter den Eichen 87, 12205 Berlin, Germany

ARTICLE INFO

Article history:
Received 20 September 2020
Revised 7 December 2020
Accepted 17 January 2021
Available online 26 January 2021

ABSTRACT

Phase diagrams are the roadmaps for designing bulk phases. Similar to bulk, grain boundaries can possess various phases, but their phase diagrams remain largely unknown. Using a recently introduced density-based model, here we devise a strategy for computing multi-component grain boundary phase diagrams based on available bulk (CALPHAD) thermodynamic data. Fe-Mn-Cr, Fe-Mn-Ni, Fe-Mn-Co, Fe-Cr-Ni and Fe-Cr-Co alloy systems, as important ternary bases for several trending steels and high-entropy alloys, are studied. We found that despite its solute segregation enrichment, a grain boundary can have lower solubility limit than its corresponding bulk, promoting an interfacial chemical decomposition upon solute segregation. This is revealed here for the Fe-Mn-base alloy systems. The origins of this counter-intuitive feature are traced back to two effects, *i.e.*, the magnetic ordering effect and the low cohesive energy of Mn solute element. Different aspects of interfacial phase stability and GB co-segregation in ternary alloys are investigated as well. We show that the concentration gradient energy contributions reduce segregation level but increase grain boundary solubility limit, stabilizing the GB against a chemical decomposition. Density-based grain boundary phase diagrams offer guidelines for systematic investigation of interfacial phase changes with applications to microstructure defects engineering.

1. Introduction

As said by Colin Humphreys, crystals are like people: it is the defects in them which tend to make them interesting! 'Playing with defects' [1] is being explored as a strategy to tailor materials properties. Grain boundaries (GBs) are one of the playable crystal defects with substantial effects on the properties of polycrystalline microstructures [2,3]. When interacting with solute atoms, GBs can mediate a whole different sort of interfacial phenomena such as intergranular premelting [4] and phase transformation [5,6]. Recent studies suggest that controlling chemical segregation at GBs can open possibilities for manipulating secondary-phase nucleation [7–9] and tuning the mechanisms of stabilizing nanostructured alloys [10,11]. Hence, GB engineering can also portray a way of tailoring alloy microstructures.

In material science, phase diagrams are the roadmaps for understanding and designing bulk phases. Such diagrams for GBs are highly desirable to exploit the potentials of GB segregation engineering for microstructure design. The start point of GB phase diagrams is the GB thermodynamics. The efforts in this direction date back to the Gibbs adsorption model [12], Langmuir-McLean model for ideal solutions [13], and Fowler-Guggenheim model for regular binary solutions [14]. Significant progress was made since then in understanding GB phenomena using, for instance, the mean-field geometrical considerations of GB structures and the force-balance models for interfacial interactions (see [15–17] and references therein). An advance in developing GB phase diagram is the λ-diagram which enables predicting the trends in GB disordering and premelting in alloys [18,19].

To account for the through-thickness inhomogeneities of interfaces, van der Waals [20] and Cahn and Hilliard [21] worked out functional free energy formulations, with nonlocal energy contributions. Due to this intrinsic feature, GB phases are also termed as 'complexions' to distinguish them from homogeneous bulk phases [22,23]. The significance of nonlocal energy contributions in stabilizing interfacial phases was discovered by Cahn [24] in studying critical point wetting. Using a crystallinity order parameter, Tang *et al.* [25,26] further developed the Cahn's formulation for studying GB premelting. This model predicts a range of phe-

* Corresponding author.
E-mail addresses: reza.kamachali@bam.de, reza.kamachali@gmail.com (R. Darvishi Kamachali).

https://doi.org/10.1016/j.actamat.2021.116668

nomena from continuous premelting to a first-order wetting transition. Mishin *et al.* [27] developed an alternative phase-filed model with three order parameters for studying premelting in Cu-Ag alloy system. Other phase-field models focusing on solute segregation at GBs were developed as well. Inspired by mean-field models [28,29], Ma *et al.* [30] used the atomic coordination number to describe GB region and investigated the effect of concentration gradient energy on solute segregation transition and drag. This model has been further extended by Mishin [31]. Heo *et al.* [32] investigated the effect of elastic interactions on GB segregation and solute drag. Kim *et al.* [33] discussed the application of an equal chemical potential condition as a degree of freedom in a phase-field model for GB segregation. As analyzed by Luo [34], various models of GBs have their advantages and shortcomings. Concerning GB thermodynamics in engineering alloys, a quantitative free energy functional for multi-component alloy systems is yet to be explored. Here the difficulty comes with the fact that before a compositional description of GB, one needs dealing with five macroscopic parameters and three microscopic states to characterize its crystallographic state. On top, the chemical and/or structural states of the GB can change under applied thermodynamic potentials *e.g.* pressure and chemical potentials [35]. These complications make it almost impossible to compute GB phase diagrams in such multi-dimensional space, not to mention GBs can also have meta-stable states [36]. Therefore, one question arises: Is it possible to have a parameter that is simple enough to construct GB phase diagrams in multi-component alloy systems, but sophisticated enough to capture essential GB properties in a general manner?

One way to simplify GB description is to view it with reference to its corresponding bulk phase, as a *lesser dense, defected* structure; using this concept, recently a density-based model has been derived to assess GB thermodynamics based on available bulk thermodynamic data [37,38]. In this model, a mesoscale atomic density field (the number of atoms per unit volume) and its spatial variations were employed to describe GB region with reference to the adjacent defect-free bulk. The nonlocal gradient energy terms here have the same application as in previous models in describing interfacial inhomogeneities. The atomic density field can be related to the crystallinity order parameter [26] or phase-field order parameters [27,32,33]. Direct use of the atomic density field, however, has the advantage that it can be calculated straight from atomistic simulations, recently demonstrated in [38]. Such connection across the length scales enabled calibration of the model parameters using atomistic calculations. The density-based model can be viewed as a generalization of the model by Ma *et al.* [30], where the discrete coordination number is replaced by the continuum atomic density field. Similar to the coordination number, the atomic density parameter can be incorporated into the CALPHAD thermodynamic framework [39,40]. Successful coupling of the density-based model with CALPHAD databases and atomistic simulations has enabled consistent explanation of experimentally observed segregation behavior in binary Fe-Mn system [38] and a FeMnNiCrCo high-entropy alloy [41].

In this work, we extend the density-based model to multi-component substitutional solid solutions and devise a strategy for building ternary GB phase diagrams. We study five Fe-Mn- and Fe-Cr-base alloy systems, *i.e.*, Fe-Mn-Cr, Fe-Mn-Ni, Fe-Mn-Co, Fe-Cr-Ni and Fe-Cr-Co alloy systems, as important ternary bases for trending steels and high-entropy alloys. In the view of our results, the origins of segregation–assisted interfacial decomposition in the ternary Fe-Mn-base systems are revealed and elaborated. We study the interfacial phase stability and GB co-segregation in these alloys. The density-based GB phase diagrams offer a simple, pragmatic framework to get the feel for essential GB phase properties, *i.e.*, its solubility and phase decomposition behavior, based on available bulk thermodynamic data. These open new perspectives for manipulating GBs in multi-component engineering alloys.

2. Methods

2.1. Multi-component density-based free energy

GBs are inhomogeneous structures with lower atomic densities compared to their corresponding bulk phase. Considering small atomic density variations in the GB region, the relative atomic density ρ can be used as a mean-field parameter to approximate a density-based Gibbs free energy density for a pure substance

$$G_i(\rho) = \rho^2 E_i^B + \rho(K_i^B + pV_i^B - TS_i^B) + \frac{\kappa_i^\rho}{2}(\nabla\rho)^2. \quad (1)$$

Here $\rho \in [\rho^{GB}, 1]$ is a dimensionless field variable, with $\rho = 1$ for the bulk and $\rho = \rho^{GB}$ at the GB-plane. κ_i^ρ is the atomic density gradient coefficient. The dependencies of G_i on the temperature and pressure are embodied in E_i^B, K_i^B, pV_i^B and TS_i^B which are the potential energy, kinetic energy, mechanical work and entropic energy density, respectively. A convention is followed here —the superscript B is used to index homogeneous bulk phase and the subscript i indexes the chemical substance. In this picture, we approximate the GB's high-dimensional crystallographic degrees of freedom with the mean-field density parameter. On top of that, the spatial density gradients, here limited to the second-order, account for the nonlocal energy contributions due to the structural inhomogeneity through the GB region. A detailed derivation of the density-based model can be found in Ref. [37].

For a N-component alloy system, we cast the density-based free energy into the conventional thermodynamic formalism for alloy mixtures as commonly used in CALPHAD approaches [39]. To account for the chemical inhomogeneity through the GB region, we further consider the Cahn-Hilliard's concentration gradient energy term [21]. Thus, the density-based Gibbs free energy as a function of solute mole fractions $\mathbf{X} = \{X_i, X_j, ..., X_N\}$ and ρ can be written as

$$G(\rho, \mathbf{X}) = \sum_i^N X_i G_i(\rho) + \rho^2 \Delta H_{mix}^B(\mathbf{X}) - T\Delta S_{mix}^B(\mathbf{X}) + \sum_i^{N-1} \frac{\kappa_{X_i}}{2}(\nabla X_i)^2 \quad (2)$$

that approximates the Gibbs free energy density of a substitutional GB solution with an atomic density $\rho < 1$ based on the bulk thermodynamic data. The concentration gradient energy coefficients κ_{X_i} are considered with respect to the solvent atoms. When $\rho = 1$ and all gradient terms vanish, it is clear that the model reduces to the homogeneous bulks, $G_i(\rho = 1) = G_i^B$ and $G(\rho = 1, \mathbf{X}) = G^B(\mathbf{X})$. The input bulk thermodynamic values can be obtained from CALPHAD databases while the gradient energy coefficients need to be calculated, as described in the following. Eq. (2) can be used as a basis for thermodynamic assessment of GBs.

2.2. Calculation of equilibrium segregation profiles

Using Eq. (2), the variational derivatives of the Gibbs free energy functional $\mathcal{G} = \int G(\rho, \mathbf{X})\, dV$ with respect to the concentration and atomic density fields give the corresponding potentials $\mu_i = \frac{\delta \mathcal{G}}{\delta X_i}$ and $\mu_\rho = \frac{\delta \mathcal{G}}{\delta \rho}$. For a system at equilibrium, we solve for the coupled differential equations

$$\Delta\mu_i(\rho, \mathbf{X}) - \Delta\mu_i(\rho = 1, \mathbf{X}^B) = 0 \quad (3)$$

and

$$\mu_\rho(\rho, \mathbf{X}) = 0 \cdot \quad (4)$$

For the Fe-base systems studied here, $\Delta\mu_i = \mu_i - \mu_{Fe}$ is the relative diffusion potential for solute species i:

$$\Delta\mu_i(\rho,\mathbf{X}) = G_i(\rho) - G_{Fe}(\rho) + \rho^2 \frac{\partial \Delta H^B_{mix}(\mathbf{X})}{\partial X_i} - T\frac{\partial \Delta S^B_{mix}(\mathbf{X})}{\partial X_i} - \kappa_{X_i}\nabla^2 X_i \quad (5)$$

where X_{Fe} is eliminated by $\sum_i^N X_i = 1$. The diffusion potential for the density parameter is

$$\mu_\rho(\rho,\mathbf{X}) = \sum_i^N X_i\left[2\rho E^B_i + K^B_i + pV^B_i - TS^B_i\right] - \sum_i^N X_i\ \kappa^\rho_i\nabla^2\rho_i + 2\rho\Delta H^B_{mix}(\mathbf{X}). \quad (6)$$

To solve Eqs. (3) and (4), a relaxation scheme is developed and implemented in an OpenMP parallel C++ code. Here we take a finite difference approach with dx = 0.1 Å and an adaptive time stepping, assuming infinitely large bulk phases, *i.e.* a constant concentration boundary condition parallel to the GB-plane while other boundaries were periodic.

We use the Thermo-Calc TCFE9 database to extract the bulk thermodynamic data. All calculations were done for T = 723 K (450°C). In order to obtain the potential energies E^B_i with reference to the bulk materials, we made a linear approximation based on the cohesive energy such that the cohesive energy difference between the bulk and a GB with atomic density ρ reads

$$E^{coh}_i(\rho = 1) - E^{coh}_i(\rho) = E^B_i\ (1-\rho)\ . \quad (7)$$

For a given interatomic potential, the cohesive energy can be calculated as a function of the interatomic distance r. The interatomic distance can be further related to the atomic density ρ by $\rho = \frac{r_0^3}{r^3}$ where r_0 is the value for the bulk phase. Three interatomic potentials which give E^{coh}_{Fe} close to the experimental value were used [42]. Here $r_0 = 2.5$ Å that corresponds to the lattice constant of $a_0 = 2.88$ Å for BCC-Fe at 723 K. We fit the $E^{coh}_{Fe}(\rho) - E^{coh}_{Fe}(\rho = 1)$ as a function of $1-\rho$ (See Fig. S7 for more details.), the slope of which gives the potential energy, used in Eqs. (7) and (1). E^B_{Fe} is determined to be −0.8 eV per atom. For other elements, E^B_i is scaled with the value of Fe by the cohesive energy ratio, *i.e.* $E^B_i = \frac{E^{coh}_i}{E^{coh}_{Fe}}E^B_{Fe}$, where the cohesive energy values are taken from [43]. For a given GB, the κ^ρ_{Fe} is then set according to the GB energy $\gamma = \frac{\pi}{4V_m}\sqrt{-2E^B_{Fe}\kappa^\rho_{Fe}}(1-\rho^{GB})^2$ [37,38]. For $\rho^{GB} = 0.9$ and GB energy $\gamma \sim 0.2$ J m^{-2}, $\kappa^\rho_{Fe} = 2.0\times10^{-13}$ J m^2 mol^{-1} is set. For the sake of simplicity, the same value is used for other elements as well.

The concentration gradient energy coefficient κ_{X_i} for each solute atom i is assessed based on its corresponding Fe-base binary mixture. As shown by Cahn and Hilliard [21], this can be related to the phase-separated interfacial energy

$$\gamma^I_i = \sqrt{2\kappa_{X_i}}\int_{X_i^{low}}^{X_i^{high}}\sqrt{\Delta G(X_i)}\,dX_i \quad (8)$$

where X_i^{low} and X_i^{high} are the limiting compositions on the miscibility gap. $\Delta G(X_i)$ is the molar free energy difference between a homogeneous alloy and the phase-separated mixture given by the common-tangent construction. For simplicity, we assume that κ_{X_i} does not depend on the concentration. Discretized $\Delta G(X_i)$ values with $dX_i = 1\times10^{-3}$ are retrieved from TCFE9 database and γ^I_i is set to be 0.01 J m^{-2}. For this interfacial energy, we obtain $\kappa_{Cr} = 1.6\times10^{-17}$ J m^2 mol^{-1} and $\kappa_{Mn} = 1.0\times10^{-16}$ J m^2 mol^{-1}. As the Eq. (8) only applies to systems with a miscibility gap. For the sake of simplicity, here we use the same gradient energy coefficient value as for Mn for Co and Ni in Fe-Co and Fe-Ni alloy systems that do not have a miscibility gap. The gradient energy coefficients can be also calculated from experiments [44], atomistic simulations [45,46] or coarse-grained bond models [47,48]. The parameters used in this work are summarized in Table 1.

Table 1
List of input parameters. All bulk related input values are taken from Thermo-Calc databas TCFE09. 1eV per atom is equal to 96.49 kJ mol^{-1}.

ρ^{GB}	0.9	dimensionless
κ^ρ	2.0×10^{-13}	J m^2 mol^{-1}
κ_{Mn}	1.0×10^{-16}	
κ_{Cr}	1.6×10^{-17}	
κ_{Co}	1.0×10^{-16}	
κ_{Ni}	1.0×10^{-16}	
E^B_{Fe}	−77.2 (−0.8)	kJ mol^{-1} (eV per atom)
E^B_{Mn}	−53.1 (−0.55)	
E^B_{Cr}	−74.3 (−0.77)	
E^B_{Co}	−79.12 (−0.82)	
E^B_{Ni}	−80.1 (−0.83)	

2.3. Calculation of miscibility gaps

We use a robust convex hull algorithm with a public package qhull wrapped by Python [49] to calculate the phase diagrams. The method is similar to those in [50,51]. For a ternary system, first we discretize the composition space into small equilateral triangles and make an approximation of the free energy function, which can be achieved using available bulk thermodynamic databases. We construct the convex hull of the discretized free energy function and then project it back onto the composition space. Three different types of the projected triangles appear: triangles with three short sides, triangles with two elongated sides, and triangles with three elongated sides can be identified. As explained by Wolff *et al.* [51], the three different types of triangles correspond to a single phase regions, two-phase regions, and three-phase regions, respectively. For two-phase regions, the two long sides of the projected triangle are approximations for the tie-lines. In practice, we project the elongated triangles into straight lines by reducing the shortest sides into a point. An example map of such triangles and the resulting miscibility gaps are shown in Figure S8 and S9, respectively. The application of the multicomponent density-based model to several Fe-base ternary systems are presented and discussed in the following.

3. Results

3.1. GB phase diagram construction: Fe-Mn-Cr system

A GB only exists together with its abutting bulk phase. For an infinitely large bulk phase, the equilibrium state of the GB is then determined through its equilibrium with the bulk phase. This is fulfilled by the equal diffusion potential condition $\Delta\mu^{GB}_i = \Delta\mu^B_i$, *i.e.* the parallel tangent construction, with $\Delta\mu_i = \mu_i - \mu_0$ where μ_0 is the potential of the solvent element, here Fe. Similarly, we solve for the equilibrium condition with respect to the atomic density ρ, $\mu_\rho = 0$ for a GB in contact with an infinitely large bulk phase. In this study, we assume a general high-angle GB so that the elastic interactions due to the dislocations can be neglected and a uniform average atomic density can be considered within the GB-plane. An average representative GB density $\rho^{GB} = 0.9$ is used. This value, however, can be determined from atomistic simulations for any given GB. We study this GB in five ternary Fe-Mn- and Fe-Cr-base systems at a $T = 723.15$ K (450 °C). Unless mentioned otherwise, only the ferritic phase will be discussed in this study.

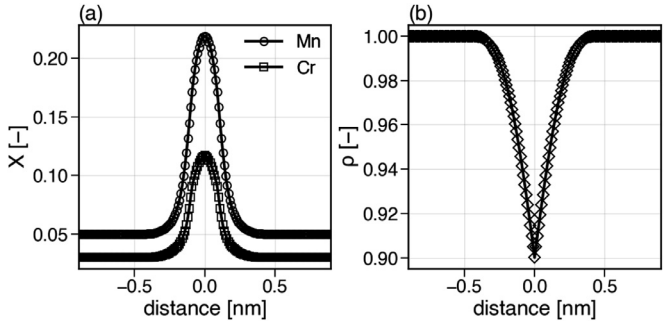

Fig. 1. 1-D Equilibrium profiles across GB region. Equilibrium (a) solute concentrations and (b) density profiles are shown for a GB with $\rho^{GB} = 0.9$ (at the GB-plane) in Fe-5Mn-3Cr (at.%) alloy at 450°C. Mn and Cr co-segregate to the GB. The density parameter is dimensionless and normalized with the bulk density.

The bulk thermodynamic data are retrieved from the Thermo-Calc TCFE9 database via the TQ-interface. For more details see Methods section.

Here we first study the Fe-Mn-Cr system as our main example. Fig. 1 depicts exemplar 1-D equilibrium profiles through the GB in a bulk Fe-5Mn-3Cr (at.%) alloy. More examples are presented in the Supplementary Information, Fig. S1. Under the equilibrium condition, the model reveals that both Mn and Cr segregate to the GB. The atomic density profile slightly extends upon the segregation which reflects coupled compositional/structural evolution in the GB region (later discussed in the following for Fig. 4(c) and (d)). As the GB-plane at $x = 0$ is approached, the concentrations of both Mn and Cr increase up to ~25 and ~12 at.%, *i.e.* ~5× and 4× their corresponding values in the abutting bulk, respectively, Fig. 1(a). The composition at the GB-plane is taken as the 'GB composition'.

We can divide the density-based Gibbs free energy density, Eq. (2), into the local and nonlocal energy contributions:

$$G(\rho, \mathbf{X}) = G^{local} + G^{nonlocal} \tag{9}$$

with

$$G^{local} = \sum_{i}^{N} X_i \left[\rho^2 E_i^B + \rho(K_i^B + pV_i^B - TS_i^B)\right] + \rho^2 \Delta H_{mix}^B(\mathbf{X}) - T\Delta S_{mix}^B(\mathbf{X}) \tag{10}$$

and

$$G^{nonlocal} = \sum_{i}^{N} X_i \frac{\kappa_i^\rho}{2}(\nabla\rho_i)^2 + \sum_{i}^{N-1} \frac{\kappa_{X_i}}{2}(\nabla X_i)^2. \tag{11}$$

The local part of the free energy density G^{local} allows an approximation of a homogeneous solid solution with a given density ρ, while the nonlocal free energy density $G^{nonlocal}$ accounts for the structural and chemical inhomogeneities across a GB.

We worked out a two-step strategy for computing GB phase diagram. In the first step, we use G^{local} and obtain the two-phase region for a hypothetically (standalone) homogeneous GB of a given density ρ —to construct the Gibbs free energy of such hypothetical GB is extremely useful in understanding the GB thermodynamic properties, especially its solubility and phase separation behavior. The bulk Fe-Mn-Cr alloy system has a large miscibility gap that is reflected as a large two-phase region in its phase diagram. The miscibility gap and tie-lines are obtained based on the convex hull construction as detailed in the Methods section. The isotherm sections of the bulk and GB, $\rho = 1$ and $\rho = 0.9$, are shown in Fig. 2(a). The region surrounded by gray lines is the two-phase region of the bulk and the black lines define the two-phase region for the GB. The tie-lines are plotted for the GB two-phase region and the inset panel shows the tie-lines in the bulk phase diagram.

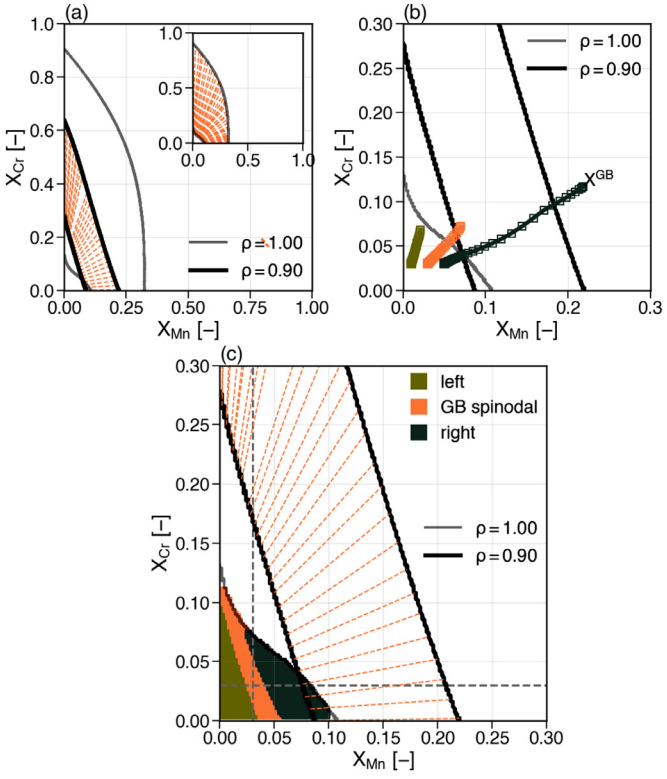

Fig. 2. Building GB phase diagram for Fe-Mn-Cr. (a) The miscibility gaps are computed for bulk ($\rho = 1$) and GB ($\rho = 0.9$). The orange dash lines are the tielines for the GB two-phase region. (b) The solute concentration profile across the GB, $(X_{Mn}(x), X_{Cr}(x))$ for three alloy compositions are mapped on the composition space. The lower-left point is the bulk composition, inside the single-phase region, while the upper-right point is the GB composition. Depending on the relative position of GB composition with respect to the GB miscibility gap, three different classes are identified and highlighted in different colors as left (dark-green), inside (orange) and right (dark-blue) to the GB spinodal region. (c) Using above scheme, the full GB phase diagram can be built by screening all compositions inside the bulk single-phase region. The legends left/GB spinodal/right refer to the position of GB composition with respect to GB two-phase region in composition space.

The shape and size of the two-phase region change with the atomic density, showing interesting features. On the Fe-Cr side (the y-axis in Fig. 2(a)), as the atomic density decreases, *i.e.* for the GB, the two-phase region shrinks on both ends and thus the solubility limits of both Fe and Cr in the GB increases relative to the bulk. However, on the Fe-Mn side this is different; The two-phase region is smaller for the GB, but it also shifts to the Fe-rich side. This shift in the two-phase region (miscibility gap) leads to a lower solubility limit of Mn in the GB phase than that in the corresponding bulk. On the Mn-Cr side (not shown here) a new miscibility gap appears by decreasing the atomic density.

In the second step of our two-step strategy for computing GB phase diagram, the full GB phase diagram can be generated by adding the information on the coexistence of the GB and bulk phases at equilibrium. Here the equilibrium profiles, as exemplified in Figs. 1 and S1, are required for which we need to consider both local (G^{local}) and nonlocal ($G^{nonlocal}$) energy contributions. The procedure is as follows: For any composition in the single-phase region of the *bulk* phase diagram (the lower left corner in Fig. 2(a)), we run a 1-D simulation to obtain the equilibrium profiles. Then the solute segregation profiles across the GB are mapped in the composition space, superposed with the miscibility gaps of the bulk and GB phases. Depending on the position of the GB composition, we can index the corresponding bulk compositions for different GB states. This idea is illustrated in Fig. 2(b): For three bulk compositions Fe-1Mn-3Cr, Fe-3Mn-3Cr and Fe-5Mn-3Cr (at.%)

inside the bulk single-phase region, equilibrium concentration profiles are plotted in the composition space, three colored lines in Fig. 2(b). On each line, the lower-left end is the bulk compositions while the upper-right end is the composition at GB center plane, as labeled as X^{GB} in Fig. 2(b). Here the GB compositions (X^{GB}) lie in three different phase regions, namely, in the left side (for the Fe-1Mn-3Cr alloy), inside (for the Fe-3Mn-3Cr alloy) and in the right side (for the Fe-5Mn-3Cr alloy) of the GB two-phase region, as labeled in Fig. 2(c).

By screening the bulk compositions inside the single-phase region (with 0.2 at.% spacing), a full GB phase diagram can be constructed. The GB phase diagram for Fe-Mn-Cr system is shown in Figure 2(c). The dark-green area in the left corner indicates a single-phase bulk which will be in equilibrium with a low-segregation single-phase GB. For bulk compositions in the orange area (middle), the GB composition is stabilized into its corresponding two-phase region. This is a result of through-thickness gradient energy terms, as discussed in the following for Fig. 4. By decreasing κ_{X_i}s, the orange area shrinks, see Fig. S2 in the Supplementary Information. For higher bulk compositions (the dark-blue area), the single-phase bulk will be in equilibrium with a single-phase but high-segregation GB. Here a critical line is the interface between the orange and dark-blue areas which marks the low to high segregation transition accompanied with the interfacial spinodal decomposition, see Fig. 4 and Fig. S3 in the Supplementary Information.

3.2. GB phase diagrams for Fe-Mn-Ni, Fe-Mn-Co, Fe-Cr-Ni and Fe-Cr-Co alloy systems

We further compute the GB phase diagrams for the Fe-Mn-Ni, Fe-Mn-Co, Fe-Cr-Ni and Fe-Cr-Co systems. The results are summarized in Fig. 3. All these ternary systems show miscibility gaps in their bulk phase diagrams which are found to be extended for GBs as well. Different features of GB miscibility gaps are spotted in different systems. Unlike the Fe-Mn-Cr, the bulk miscibility gaps in these systems only exist either on the Fe-Mn or Fe-Cr side. One general observation is that the GB two-phase region in the Fe-Mn-base systems shrink and shift to the Fe-rich corner, while it rather shrinks on all three sides in the Fe-Cr-base systems. These mean that the solubility limits in Fe-Mn-base GBs are reduced on the Fe-rich corner, while the solubility limits for all binary pairs in the Fe-Cr-base GBs are increased, relative to their corresponding bulk solid solutions. For the single-phase bulks in the Fe-Mn-base systems, the GB can easily undergo the low to high segregation transition. This is indicated by the large dark-blue regions in the GB phase diagrams, Fig. 3(a) and (b). In contrast, the dark-blue areas tends to vanish for the Fe-Cr-base systems (Fig. 3(c) and (d)) indicating a small or no compositional window to complete a GB segregation transition in the presence of a single-phase bulk material.

4. Discussion

Traditionally, atomistic simulations were found to be useful in studying individual GB structures. Today, these are augmenting with the help of computational advancements that enable screening a larger range of descriptors for GBs [52,53]. A remaining challenge, however, that impedes development of GB phase diagrams is to describe GBs of various chemistry and crystallography in a general thermodynamic framework. Mesoscale models were somewhat successful in this direction providing means to predict a spectrum of interfacial phenomena [15,23,34,54]. In the density-base concept, a mean-field philosophy is adopted into a mesoscale phase-field framework [37]. Here we benefit from the strengths of both mean-field and phase-field approaches: the mean-field parameter, ρ, enables an approximation picture of the GB as a lesser dense bulk-like homogeneous material, while its spatial variations (gradients) account for GB's through-thickness structural inhomogeneity. This is then cast into the conventional CALPHAD thermodynamic model for multi-component mixtures, Eq. (2), further equipped with by concentration gradient energies.

One of the advantages of this model is that it allows us to assess GB phase diagrams based on available bulk thermodynamic data. It is obvious that one cannot reconstruct all the information with regard to the crystallographic aspects of GB phenomena based on the atomic density parameter. The combination of the GB density and the gradient energy coefficients, however, gives enough control over the GB energy and segregation behavior, which manifests itself in the equilibrium concentration/density profiles and segregation isotherms, as demonstrated recently [38].

4.1. Origins of GB solubility limits

Despite its simple nature, the results from the density-based GB phase diagrams turn to be nontrivial. This is directly reflected in both the shape and position of the two-phase region in the GB phase diagram. A common feature in all ternary systems studied here is that the miscibility gap, which is the result of competitive mixing enthalpy and entropy terms, tend to shrink for the GBs, *i.e.* when $\rho < 1$. This effect is due to the reduced coordination number and weakened atomic bonds in the lesser dense GB, which reduce the GB mixing enthalpy by $(1-\rho^2)\Delta H^B_{mix}$. For a lower GB density, a larger deviation from the bulk mixture behavior is expected. In addition to this shrink, the two-phase region in the GB phase diagram can also shift in the composition space. This is prominent in the Fe-Mn-base systems (Fe-Mn-Cr, Fe-Mn-Ni and Fe-Mn-Co) for which the GB two-phase regions shift to the Fe-rich corner, Figs. 2(c), 3(a) and (b). For the GB, this means a lower solubility limit, which can be an amplifying factor in activating interfacial phase decomposition. In contrast, the GBs in Fe-Cr-base alloys (Fe-Cr-Ni and Fe-Mn-Co) show higher solubility limits than the bulk, Figs. 3(c) and (d). This means that in these system the GB capacity to accommodate solute atoms is higher than bulk and thus an interfacial chemical decomposition can only occur for segregation levels exceeding the single-phase bulk compositions.

The shrink and shift of the interfacial miscibility gaps in the Fe-Mn-base systems are mainly due to the magnetic ordering effect in the Fe-Mn side [55,56]. With no or little contribution from magnetic ordering, the bulk would have regular, more symmetric mixing enthalpy (and two-phase region) over the composition space. This will be then inherited by the GB, taking a similar symmetric miscibility gap, only with different dimensions. The Fe-Cr-Ni and Fe-Cr-Co systems here show this trend, where the GB two-phase region shrinks rather uniformly inside the bulk two-phase region. In the presence of the magnetic ordering, however, the symmetry of the mixing curves and two-phase region in the phase diagram breaks [57]. These are shown for Fe-Mn solid solution in Figs. S4 and S5 in the Supplementary Information. As a result, the GB two-phase regions for the Fe-Mn-Cr, Fe-Mn-Ni and Fe-Mn-Co systems shrink and shift in an asymmetric manner, Fig. 2(c) and Fig. 3(a) and (b).

These observations predict that a system with asymmetric mixing enthalpy and thus asymmetric miscibility gap could be potentially prone to an interfacial spinodal decomposition. An instance of interfacial phase decomposition is experimentally evidenced when studying binary Fe-Mn alloys with 3 to 9 %Mn content [8,38]. Based on the asymmetry argument, the binary Co-Mn can be proposed for potential interfacial phase decomposition. The binary Fe-Mn, Fe-Cr and Co-Mn bulk phase diagrams are compared in the Supplementary Information, Fig. S5. As the asymmetry effect comes from the magnetic ordering, it can open an avenue for controlling GB segregation engineering by applying an external mag-

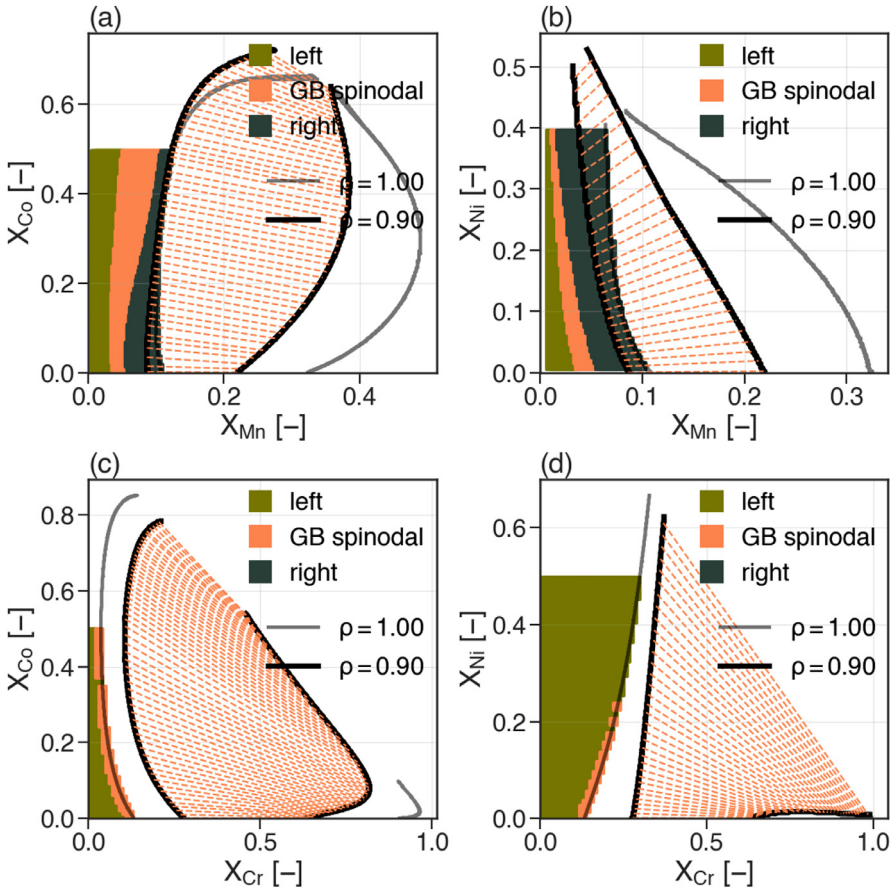

Fig. 3. GB phase diagrams for Fe-Mn- and Fe-Cr-base alloys. For a GB with $\rho^{GB} = 0.9$ at 450°C the GB phase diagram for (a) Fe-Mn-Co, (b) Fe-Mn-Ni, (c) Fe-Cr-Co and (d) Fe-Cr-Ni systems are obtained. The gray and black lines show the bulk and GB two-phase regions, respectively. The left/GB spinodal/right refer to the position of GB composition with respect to GB two-phase region in composition space. For the Fe-Mn-base systems the GB miscibility gaps shift to the left, lowering the GB solubility limits. In contrast, the GB solubility limits in the Fe-Cr-base systems increase.

netic field. These observations can be considered along recent discussions around the role of external magnetic fields on the evolution of defect structures [58]. It is worth noting that here the elastic interactions between GB and solute atoms are not considered. Such elastic interactions, that can be important in studying interstitial solute atoms and/or low-angle GBs, are left for a future study.

Apart from the mixing enthalpy, the bonding energies of the pure elements can have a profound effect on the coexistence of the GB and bulk phases. The energy difference between the (pure) solvent and solute regulates the constant value $G_i(\rho) - G_{Fe}(\rho)$ in the chemical potential, Eq. (5), which directly affects equilibrium compositions of the coexisting GB and bulk phases. Figure S6 in the Supplementary Information compares the bulk and GB chemical potential curves for Mn and Cr in the Fe-Mn-Cr system. In the presence of an interfacial phase separation, the corresponding difference between the bulk and GB chemical potential curves, *i.e.*, the vertical shift as much as $G_i(\rho) + G^B_{Fe} - G_{Fe}(\rho) - G^B_i$, increases the possibility for have single-phase bulk alloys in equilibrium with two-phase GBs. In a pure substance, the energy variation across the GB builds into the GB energy, $\gamma_i = \int (G_i(\rho) - G^B_i)\ \mathrm{d}V$, and the ideal segregation isotherm discussed by Langmuir-McLean [13]. The main contribution to the ideal segregation energy comes from the term $(1-\rho^2)\Delta E^B_i$, that is, the difference in the solute and solvent potential energies.

It has been shown that the GB energies of BCC metals often scales with their cohesive energy ratio [59]. The cohesive energies of Fe, Mn and Cr are 4.28, 2.92 and 4.10 eV/atom, respectively [43]. The cohesive energy difference between the Fe and Mn (1.36 eV/atom) is therefore much greater than that between the Fe and Cr (0.18 eV/atom). This means that a given GB structure is likely to have much less GB energy when, instead of the Fe atoms, it could be 'made of' Mn atoms, $\gamma_{Mn} << \gamma_{Fe}$. The difference between γ_{Cr} and γ_{Fe}, however, can be rather small, resulting in lower driving forces for segregation. The small cohesive energy of Mn together with its increasingly limited solubility in GBs (due to the magnetic ordering effect) make the Fe-Mn-Cr, Fe-Mn-Ni and Fe-Mn-Co alloy systems exceptionally susceptible to solute segregation and interfacial phase decomposition. Accordingly, a supervised screening of the relative cohesive energies and mixing enthalpies of mixtures can guide a search for similar systems.

4.2. GB spinodal and effects of gradient energies

Segregation–assisted GB phase decomposition is considered as a means for tailoring the properties of a microstructure by boosting and/or controlling the potential intergranular phase transformations. Fig. 4(a) and (b) show examples of Mn and Cr segregation isotherms in the Fe-Mn-Cr systems with the other species in the bulk being fixed at 3 at.%, respectively. The jumps in the isotherms indicate the segregation–assisted interfacial phase separation at the GB. This is accompanied with a change in the atomic density variation that is due to the coupled evolution of the atomic density and concentration fields. The corresponding atomic density variations in the GB region are shown in Fig. 4(c) and (d). Our results show that the jumps in the segregation isotherms correspond

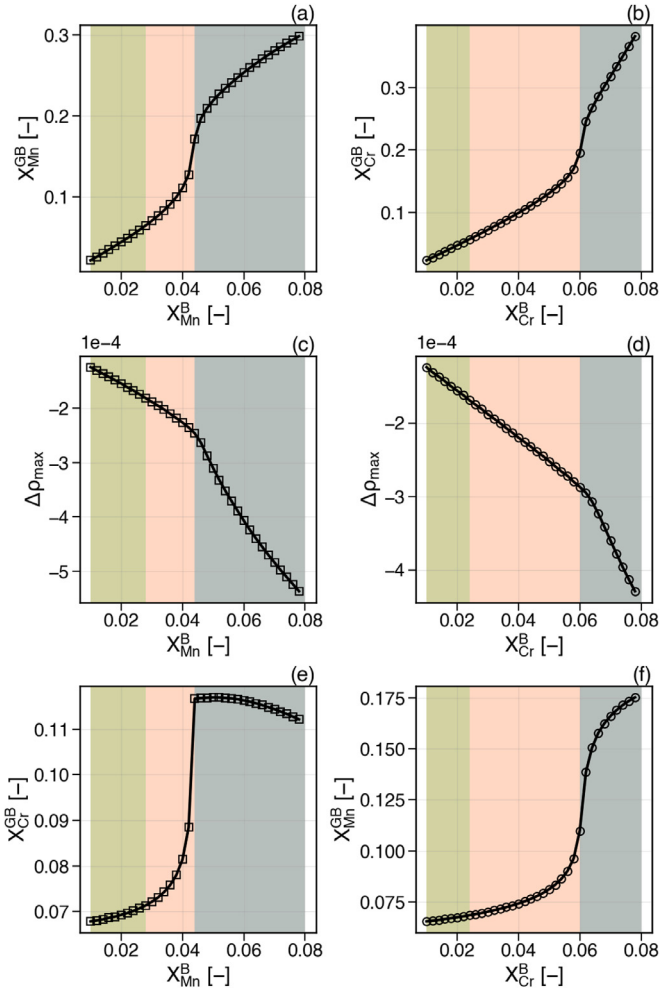

Fig. 4. GB segregation isotherms and segregation-related density variations in Fe-Mn-Cr alloys. (a)(c)(e), the left column, summarize the the results when the bulk composition of Mn is varied while Cr is fixed at 3.0 at.%. (b)(d)(f), the right column, correspond to the case where Cr is varied while Mn is fixed at 3.0 at.%. (a), GB segregation isotherm of Mn. (b), GB segregation isotherm of Cr. (c), maximal density variation (relative to the density profile with no segregation) in GB regions as a function of bulk composition of Mn. (d), maximal density variation in GB regions as a function of bulk composition of Cr. (e), the composition of Cr at GBs as a function of the bulk composition of Mn. (f), the composition of Mn at GBs as a function of the bulk composition of Cr. The background colors correspond to three colored regions in the phase diagram, Fig. 2(c).

to the interface between the orange and dark-blue areas in the GB phase diagram, Figs. 2(c), at which the GB decomposes spinodally while the bulk remains a single-phase solid solution. We also found that the stretch in the segregation isotherm over the jump composition originates in the gradient energy contributions to the chemical potential, $\sum \kappa_{X_i} \nabla^2 X_i$, which resist compositional discontinuity through the GB region.

To test this idea, we studied the Fe-Mn-Cr system with several combinations of $\kappa_{X_{Mn}}$ and $\kappa_{X_{Cr}}$ values. Figure S2 in the Supplementary Information shows that as the concentration gradient energy coefficients decrease, the orange intermediate area in the GB phase diagram sharpens and shifts to the left. The corresponding segregation isotherms are presented in Fig. S3. When the concentration gradient energy coefficient increases, the level of GB segregation decreases, reducing gradient energies by lowering concentration gradients across the GB. At the same time, a higher gradient energy coefficient shifts the GB solubility to higher values. This is because of the gradient energies producible by an interfacial phase decomposition that can be prevented by stabilizing the single-phase GB

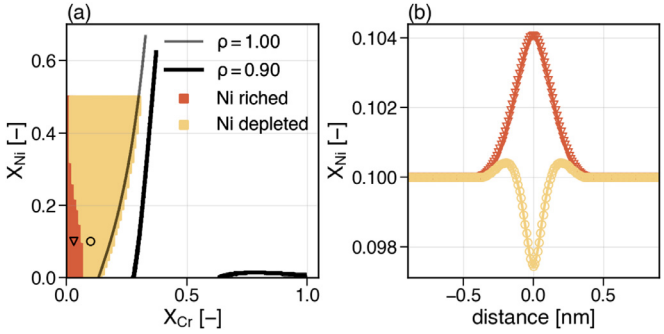

Fig. 5. Ni Segregation in Fe-Cr-Ni alloys. (a) Ni segregation map and (b) typical segregation profiles showing Ni enrichment, marked by ∇ and depletion, marked by o. For high-Cr Fe-Cr-Ni bulk, Ni depletes from GB region.

to a higher concentration level, *i.e.* higher GB solubility. These findings confirm Cahn's original discovery of the conditional extended stability of a wetting layer [24] and further emphasize the significance of nonlocal gradient energy terms and their role in controlling interfacial segregation and solubility.

For bulk alloy compositions laying in the dark-blue area of the GB phase diagram, an unsegregated GB can undergo a transient segregation–assisted phase separation (for a finite period of time) [38]. During this process, the GB enriches to the unstable two-phase region and spontaneously decompose into low- and high-segregation islands. The segregation then proceeds until the equilibrium GB segregation is achieved. Using Eq. (2), the temporal aspects of the transient spinodal phenomenon can be assessed now in multi-component systems that gives insights for designing optimal heat treatments. The dynamics of segregation and interfacial phase decomposition in multi-component alloy systems therefore desires further studies left for a future work.

4.3. Co-segregation in ternary alloys

Guttmann noted that depending on the nature of solute-solute interactions, a range of GB co-segregation behavior can be expected in multi-component alloy systems [60]; an attractive chemical interaction results in enhanced co-segregation whereas a repulsive interaction may suppress co-segregation or cause desegregation of one (or more) solute species. Such co-segregation behavior can extend beyond the GBs as well, e.g. for staking faults [61]. The co-segregation isotherms for Cr and Mn in the Fe-Mn-3Cr and Fe-3Mn-Cr systems are shown in Fig. 4(e) and (d), respectively. These results show that the Mn and Cr drag each other into the GB region, even showing co-segregation jumps. The effects of Mn and Cr on each other appear to be asymmetric —the Mn content in the bulk influences Cr segregation much stronger than vice versa. Another instance of enhanced co-segregation is Ni segregation in Fe-Mn-3Ni systems which rises higher when the Mn content in the bulk increases. The results are shown in the Supplementary Information, Fig. S1. In contrast, higher amounts of Mn and Cr in the Fe-Mn-3Co and Fe-Cr-3Co amplify the depletion (desegregation) of Co at the GB. An interesting co-segregation behavior was found in the Fe-Cr-Ni system: While Cr is always enriched at the GB, Ni atoms can show both depletion and enrichment depending on the Cr content in the alloys. Alloy compositions with Ni-depleted and Ni-enriched GBs are mapped on the GB phase diagram, Fig. 5 (a). Examples of equilibrium Ni concentration profile are shown in Fig. 5 (b). Experimental evidences of GB segregation in 304SS stainless steel shows that in the presence of Cr, GBs can be depleted from Ni [62]. The repulsive segregation of Ni and Cr atoms is also observed in high-entropy alloys [41], suggesting

the segregation competition between Cr and Ni beyond the body-centered cubic structure as well.

5. Summary

In this study, we devise a density-based approach for computing ternary GB phase diagrams based on available bulk thermodynamic data. Using the GB phase diagrams, a range of interfacial phenomena in Fe-Mn- and Fe-Cr-base alloy systems were predicted. For Fe-Mn-Cr, Fe-Mn-Ni and Fe-Mn-Co systems, we found that, despite the GB segregation enrichment, GB can attain a lower solubility limit than that of the corresponding bulk phase while the opposite case is observed in the Fe-Cr-Ni and Fe-Cr-Co systems (Figs. 2 and 3). We show that (i) the magnetic ordering effect, causing an asymmetric shift in the GB miscibility gap, and (ii) the low cohesive energy of Mn compared to Fe, resulting in a vertical shift in its chemical potential surface, govern the extended interfacial phase decomposition and limited interfacial solubility revealed in the Fe-Mn-base systems. We also found that higher gradient energy contributions increase GB's solubility limit, in accord with Cahn's prediction [24], but suppresses GB's segregation level stabilizing it against interfacial chemical decomposition. The GB phase diagrams here provide a perspective on how to screen for potential systems prone to segregation and consequent interfacial spinodal. In this study, we focused on the general high-angle GBs and substitutional solid solutions. Further consideration of elastic interactions is required to enable studying low-angle GBs and interstitial solute atoms. Despite its limitations, density-based GB phase diagram offers a simple, pragmatic framework for understating GB phase equilibria which is crucial to facilitate defects engineering in heterogeneous microstructures. A further development of GB phase diagram to more complex alloys is viable, for instance, by coupling the density-based thermodynamic concept with the tensor completion techniques [63].

Data availability

Further data and codes of this study are available per reasonable request.

Declaration of Competing Interest

The authors declare that they have no known competing financial interests or personal relationships that could have appeared to influence the work reported in this paper.

Acknowledgments

The current research is being conducted within the project DA 1655/2-1 in the Heisenberg programme from the German Research Foundation (DFG). RDK acknowledges financial supports from the DFG within this programme as well as in projects DA 1655/1-1 and DA 1655/1-2.

Supplementary material

Supplementary material associated with this article is available in the online version, at doi:10.1016/j.actamat.2021.116668

References

[1] X. Li, K. Lu, Playing with defects in metals, Nature materials 16 (2017) 700.
[2] J. Hu, Y.N. Shi, X. Sauvage, G. Sha, K. Lu, Grain boundary stability governs hardening and softening in extremely fine nanograined metals, Science 355 (2017) 1292–1296.
[3] Z. Yu, et al., Segregation-induced ordered superstructures at general grain boundaries in a nickel-bismuth alloy, Science 358 (2017) 97–101.
[4] J. Luo, H. Cheng, K.M. Asl, C.J. Kiely, M.P. Harmer, The role of a bilayer interfacial phase on liquid metal embrittlement, Science 333 (2011) 1730–1733.
[5] K. Matsui, N. Ohmichi, M. Ohgai, H. Yoshida, Y. Ikuhara, Effect of alumina-doping on grain boundary segregation-induced phase transformation in yttria-stabilized tetragonal zirconia polycrystal, Journal of materials research 21 (2006) 2278–2289.
[6] V. Attari, S. Ghosh, T. Duong, R. Arroyave, On the interfacial phase growth and vacancy evolution during accelerated electromigration in Cu/Sn/Cu microjoints, Acta Materialia 160 (2018) 185–198.
[7] A. da Silva, et al., Phase nucleation through confined spinodal fluctuations at crystal defects evidenced in Fe-Mn alloys, Nature communications 9 (2018) 1137.
[8] A. da Silva, et al., Thermodynamics of grain boundary segregation, interfacial spinodal and their relevance for nucleation during solid-solid phase transitions, Acta Materialia 168 (2019) 109–120.
[9] M. Glienke, et al., Grain boundary diffusion in CoCrFeMnNi high entropy alloy: kinetic hints towards a phase decomposition, Acta Materialia (2020).
[10] A.J. Detor, C.A. Schuh, Tailoring and patterning the grain size of nanocrystalline alloys, Acta Materialia 55 (2007) 371–379.
[11] T. Chookajorn, H.A. Murdoch, C.A. Schuh, Design of stable nanocrystalline alloys, Science 337 (2012) 951–954.
[12] J.W. Gibbs, The Collected Works of J. Willard Gibbs, Yale University Press, London, England, 1957.
[13] D. McLean, Grain boundaries in metals, University Press, Oxford, 1957.
[14] R. Fowler, E.A. Guggenheim, Statistical thermodynamics, Cambridge University Press, 1956.
[15] P. Lejček, Grain Boundary Segregation in Metals, Springer, 2010.
[16] S. Dregia, P. Wynblatt, Equilibrium segregation and interfacial energy in multicomponent systems, Acta metallurgica et materialia 39 (1991) 771–778.
[17] P. Wynblatt, D. Chatain, Anisotropy of segregation at grain boundaries and surfaces, Metallurgical and Materials Transactions A 37 (2006) 2595–2620.
[18] X. Shi, J. Luo, Developing grain boundary diagrams as a materials science tool: A case study of nickel-doped molybdenum, Physical Review B 84 (2011) 2507–2524.
[19] N. Zhou, J. Luo, Developing grain boundary diagrams for multicomponent alloys, Acta Materialia 91 (2015) 202–216.
[20] J.D. van der Waals, The thermodynamic theory of capillarity under the hypothesis of a continuous variation of density, Journal of Statistical Physics 20 (1979) 200–244.
[21] J.W. Cahn, J.E. Hilliard, Free energy of a nonuniform system. I. interfacial free energy, The Journal of chemical physics 28 (1958) 258–267.
[22] S.J. Dillon, M. Tang, W.C. Carter, M.P. Harmer, Complexion: A new concept for kinetic engineering in materials science, Acta Materialia 55 (2007) 6208–6218.
[23] P.R. Cantwell, et al., Grain boundary complexions, Acta Materialia 62 (2014) 1–48.
[24] J.W. Cahn, Critical point wetting, The Journal of Chemical Physics 66 (1977) 3667–3672.
[25] M. Tang, W.C. Carter, R.M. Cannon, Diffuse interface model for structural transitions of grain boundaries, Physical Review B 73 (2006) 024102.
[26] M. Tang, W.C. Carter, R.M. Cannon, Grain boundary transitions in binary alloys, Physical review letters 97 (2006) 075502.
[27] Y. Mishin, W.J. Boettinger, J.A. Warren, G.B. McFadden, Thermodynamics of grain boundary premelting in alloys, I. Phase-field modeling. Acta Materialia 57 (2009) 3771–3785.
[28] P. Wynblatt, Y. Liu, Two-dimensional phase transitions associated with surface miscibility gaps, Journal of Vacuum Science & Technology A: Vacuum, Surfaces, and Films 10 (1992) 2709–2717.
[29] P. Wynblatt, A. Saúl, D. Chatain, The effects of prewetting and wetting transitions on the surface energy of liquid binary alloys, Acta materialia 46 (1998) 2337–2347.
[30] N. Ma, S.A. Dregia, Y. Wang, Solute segregation transition and drag force on grain boundaries, Acta Materialia 51 (2003) 3687–3700.
[31] Y. Mishin, Solute drag and dynamic phase transformations in moving grain boundaries, Acta Materialia 179 (2019) 383–395.
[32] T.W. Heo, S. Bhattacharyya, L.-Q Chen, A phase field study of strain energy effects on solute-grain boundary interactions, Acta Materialia 59 (2011) 7800–7815.
[33] S.G. Kim, J.S. Lee, B.J. Lee, Thermodynamic properties of phase-field models for grain boundary segregation, Acta Materialia 112 (2016) 150–161.
[34] J. Luo, Stabilization of nanoscale quasi-liquid interfacial films in inorganic materials: a review and critical assessment, Critical reviews in solid state and materials sciences 32 (2007) 67–109.
[35] T. Meiners, T. Frolov, R.E. Rudd, G. Dehm, C.H. Liebscher, Observations of grain-boundary phase transformations in an elemental metal, Nature 579 (2020) 375–378.
[36] J. Han, V. Vitek, D.J. Srolovitz, Grainboundary metastability and its statistical properties, Acta Materialia 104 (2016) 259–273.
[37] R. Darvishi Kamachali, A model for grain boundary thermodynamics, RSC Advances 10 (2020) 26728–26741.
[38] R. Darvishi Kamachali, et al., Segregation-assisted spinodal and transient spinodal phase separation at grain boundaries, npj Computational Materials 6 (2020) 1–13.
[39] N. Saunders, A.P. Miodownik, CALPHAD (Calculation of Phase Diagrams): A Comprehensive Guide, Elsevier, 1998.
[40] W. Oates, H. Wenzl, T. Mohri, On putting more physics into calphad solution models, Calphad 20 (1996) 37–45.

[41] L. Li, R. Darvishi Kamachali, Z. Li, Z. Zhang, Grain boundary energy effect on grain boundary segregation in an equiatomic high-entropy alloy, Physical Review Materials 4 (2020) 053603.
[42] NIST. Interatomic Potentials Repository.
[43] C. Kittel, Introduction to solid state physics Eighth, Wiley, New York, 1976.
[44] A.J. Ardell, Gradient energy, interfacial energy and interface width, Scripta Materialia 66 (2012) 423–426.
[45] M. Asta, J.J. Hoyt, Thermodynamic properties of coherent interfaces in fcc-based Ag-Al alloys: a first-principles study, Acta Materialia 48 (2000) 1089–1096.
[46] J. Hoyt, Molecular dynamics study of equilibrium concentration profiles and the gradient energy coefficient in Cu-Pb nanodroplets, Physical Review B 76 (2007) 094102.
[47] E.A. Lass, W.C. Johnson, G.J. Shiflet, Correlation between CALPHAD data and the cahn-hilliard gradient energy coefficient and exploration into its composition dependence, Calphad 30 (2006) 42–52.
[48] T. Barkar, L. Höglund, J. Odqvist, J. Ågren, Effect of concentration dependent gradient energy coefficient on spinodal decomposition in the fe-cr system, Computational Materials Science 143 (2018) 446–453.
[49] C.B. Barber, D.P. Dobkin, H. Huhdanpaa, The quickhull algorithm for convex hulls, ACM Transactions on Mathematical Software (TOMS) 22 (1996) 469–483.
[50] S. Mao, D. Kuldinow, M.P. Haataja, A. Košmrlj, Phase behavior and morphology of multicomponent liquid mixtures, Soft Matter 15 (2019) 1297–1311.
[51] J. Wolff, C.M. Marques, F. Thalmann, Thermodynamic approach to phase coexistence in ternary phospholipid-cholesterol mixtures, Physical review letters 106 (2011) 128104.
[52] Q. Zhu, A. Samanta, B. Li, R.E. Rudd, T. Frolov, Predicting phase behavior of grain boundaries with evolutionary search and machine learning, Nature communications 9 (2018) 1–9.
[53] L. Huber, R. Hadian, B. Grabowski, J. Neugebauer, A machine learning approach to model solute grain boundary segregation, npj Computational Materials 4 (2018) 1–8.
[54] K. . Grönhagen, J. Ågren, Grain-boundary segregation and dynamic solute drag theory - a phase-field approach, Acta Materialia 55 (2007) 955–960.
[55] M. Hillert, M. Jarl, A model for alloying in ferromagnetic metals, Calphad 2 (1978) 227–238.
[56] W. Huang, An assessment of the fe-mn system, Calphad 13 (1989) 243–252.
[57] A.P. Miodownik, The effect of magnetic transformations on phase diagrams, Journal of Phase Equilibria 2 (1982) 406.
[58] R. Backofen, K.R. Elder, A. Voigt, Controlling grain boundaries by magnetic fields, Physical review letters 122 (2019) 126103.
[59] S. Ratanaphan, et al., Grain boundary energies in body-centered cubic metals, Acta Materialia 88 (2015) 346–354.
[60] M. Guttmann, Equilibrium segregation in a ternary solution: A model for temper embrittlement, Surface Science 53 (1975) 213–227.
[61] L. Feng, Y. Rao, M. Ghazisaeidi, M.J. Mills, Y. Wang, Quantitative prediction of suzuki segregation at stacking faults of the γ phase in ni-base superalloys, Acta Materialia 200 (2020) 223–235.
[62] H. Li, S. Xia, W. Liu, T. Liu, B. Zhou, Atomic scale study of grain boundary segregation before carbide nucleation in ni-cr-fe alloys, Journal of nuclear materials 439 (2013) 57–64.
[63] Y.A. Coutinho, N. Vervliet, L. De Lathauwer, N. Moelans, Combining thermodynamics with tensor completion techniques to enable multicomponent microstructure prediction, npj Computational Materials 6 (2020) 1–11.